Supporting Information

Defect-state-controlled carrier recombination dynamics in nonmetal-doped brookite TiO_2

Yucui Xiang†[a,b], Ke Long†[a], Dazhong Sun[a], Hanling Wang[a], Daokuan Ma[a], Shiyu Zheng[a], Shuaijun Wang[c], Jinqiang Zhang*[d], Jing Fan*[e], Liyong Gan*[a,b], Xiaoyuan Zhou[a,b]

[a] College of Physics and Center of Quantum Materials and Devices, Chongqing University, Chongqing 401331, China

[b] Chongqing Institute of New Energy Storage Materials and Equipment, Chongqing 401120, China

[c] School of Energy and Power Engineering, Jiangsu University, Zhenjiang 212013, China

[d] School of Molecular Sciences, The University of Western Australia, Perth, WA 6009, Australia

[e] Center for Computational Science and Engineering, Southern University of Science and Technology, Shenzhen 518055, China

†These authors contributed equally to this work.

1. Calculation details

In this study, the Vienna Ab initio Simulation Package (VASP) was employed to perform geometry optimizations, molecular dynamics simulations, and self-consistent field calculations.[1] The exchange–correlation potential was calculated using the generalized gradient approximation (GGA) with the Perdew–Burke–Ernzerhof (PBE) functional.[2] A kinetic energy cutoff of 500 eV was applied to the plane wave basis set. For geometry optimization, a Γ-centered 3 × 3 × 3 Monkhorst–Pack k-point mesh was utilized, while a denser Γ-centered 5 × 5 × 5 k-point mesh was employed for the detailed analysis of electronic structures.[3] The electronic self-consistent field calculations were converged to an energy threshold of 10^{-5} eV, and the atomic structures were relaxed until the residual ionic forces were minimized to below 0.02 eV·Å^{-1}. To compensate for the self-interaction error associated with the DFT functional, an on-site Coulomb correction with an effective Hubbard parameter U_{eff} of 3.0 eV was applied to the Ti 3d orbitals, in accordance with previous literature.[4, 5]

Formation energies of substitutional nonmetal dopants are evaluated based on total-energy differences and element chemical potentials. In a general form:[6, 7]

$$E_{form} = E_{def} - E_{pure} - \mu_X + \mu_O \#(1)$$

where E_{def} and E_{pure} are the total energies of the defective and pristine supercells, respectively. The μ_X and μ_O are dopants (C, N, F, P, S, Cl, Se, Br and I) and O chemical potentials. The Ti and O chemical potentials satisfy the equilibrium constraint of the host TiO_2 phase, $\mu_{TiO_2} = \mu_{Ti} + 2\mu_O$. The O-rich limit is defined as $\mu_O = 1/2 E_{O_2}$, with $\mu_{Ti} = \mu_{TiO_2} - E_{O_2}$. In Ti-rich conditions, μ_{Ti} is the energy of a Ti atom in its bulk state (μ_{bulk}), and μ_O is calculated as $\mu_O = 1/2(\mu_{TiO_2} - \mu_{Ti})$. Dopant chemical potentials are referenced to their stable reservoirs as follows: $\mu_C = E_{CO_2} - 2\mu_O$, $\mu_N = 1/2 E_{N_2}$, $\mu_F = 1/2 E_{F_2}$, $\mu_P = 1/4 E_{P_4}$, $\mu_S = E_{SO_2} - 2\mu_O$, $\mu_{Cl} = 1/2 E_{Cl_2}$, $\mu_{Se} = 1/3 \mu_{Se_3}$, $\mu_{Br} = 1/2 E_{Br_2}$ and $\mu_I = 1/2 E_{I_2}$. Convergence tests are conducted using a 1 × 2 × 2 brookite TiO_2 supercell

containing 96 atoms. The optimized brookite bulk lattice parameters ($a = 9.31$, $b = 11.05$ Å and $c = 10.48$ Å) agree well with available experimental values.[8] To benchmark the thermodynamic feasibility of nonmetal substitution in brookite TiO_2, we additionally computed the formation energies of the same dopants in anatase and rutile TiO_2 and directly compared them with those in brookite. This comparison is motivated by the fact that stable nonmetal-doped anatase and rutile TiO_2 have already been realized experimentally, and thus provide practical reference phases for assessing the viability of doped brookite.[9-11] The anatase calculations were performed using a 96-atom supercell with lattice parameters $a = b = 7.81$ Å and $c = 19.37$ Å, while the rutile calculations employed a 96-atom supercell with $a = b = 9.19$ Å and $c = 11.46$ Å. The computed formation energies for brookite, anatase and rutile under O-rich and Ti-rich limits are summarized in Table S1 and compared in Fig. 1.

Ab initio molecular dynamics (AIMD) simulations are initiated from the optimized structures. The system was equilibrated at 300 K for 2 ps with a time step of 1 fs, followed by 5 ps of microcanonical (NVE) dynamics with the same time step to generate nuclear trajectories. Unless otherwise stated, all MD simulations are performed using the same supercell size as used for the formation-energy calculations. Nonadiabatic carrier dynamics are simulated using the Hefei-NAMD package with the decoherence-induced surface hopping (DISH) algorithm within a real-time time-dependent Kohn–Sham (KS) framework.[12-14] The nuclear motion is taken from the AIMD trajectories (classical-path approximation), and electronic transitions among adiabatic KS states are driven by time-dependent nonadiabatic couplings along the nuclear trajectory.[15] From the generated MD trajectory, 50 initial nuclear configurations are randomly selected from the first 1000 MD frames as starting points for independent NAMD runs. To assess the sampling convergence of the NAMD simulations, we performed a convergence test with respect to the number of initial configurations for representative Cl/TiO_2 and P/TiO_2 systems.

Different numbers of nuclear geometries were extracted from the same 5 ps NVE production trajectory and used to initialize independent NAMD simulations. As shown in Fig. S3, the fitted electron and hole lifetimes remain stable within minor fluctuations when the number of initial configurations is increased from 50 to 100, indicating that the 5 ps NVE production trajectory and 50 initial configurations provide a stable estimate of the averaged population decay and fitted lifetime for the present comparative NAMD analysis.

The PBE+U method was adopted following previous TiO_2 studies, where a Hubbard U correction on Ti 3*d* states has been used to improve the description of localized Ti 3*d* electrons in TiO_2.[4, 5] Same supercell size was used for all doped systems to ensure a consistent comparison across the full dopant series and to keep the AIMD/NAMD calculations computationally feasible, following the common practice in comparative NAMD studies. Notably, the exchange–correlation functional and supercell size in theoretical calculations may influence the calculated band gap, defect-level alignment, defect localization, NAC values and carrier lifetimes. The discussion in this work mainly focuses on the relative carrier-recombination trends among different nonmetal dopants obtained under the same PBE+U/supercell parameters.

2. Nonadiabatic coupling

In the adiabatic representation underlying surface-hopping NAMD, phonon-driven nuclear motion induces time-dependent mixing of KS states and thereby enables carrier recombination. The central quantity entering the hopping probability is the nonadiabatic coupling (NAC) between adiabatic states *i* and *j*, defined along a nuclear trajectory R as:

$$d_{ij} = < \phi_i(R) \left| \frac{\partial}{\partial t} \right| \phi_j(R) > \#(2)$$

where ϕ denotes adiabatic KS orbitals. Using the chain rule, NAC can be related to the nuclear velocities and derivative couplings:

$$d_{ij} = \dot{R} < \varphi_i | \nabla_R | \varphi_j > = \frac{< \varphi_i | \nabla_R H | \varphi_j >}{\epsilon_j - \epsilon_i} \dot{R} \#(3)$$

where H is the KS Hamiltonian, and $\dot{R}$ is the nuclear velocity vector.[12] This expression makes explicit that nonadiabatic transitions are jointly controlled by (i) the instantaneous energy difference $\epsilon_j - \epsilon_i$, the electron-phonon coupling matrix element $< \varphi_i | \nabla_R H | \varphi_j >$ and the nuclear velocity term $\dot{R}$. In practical plane-wave implementations, d_{ij} is commonly evaluated via a finite-difference form using orbital overlaps between two consecutive MD frames, which provides a numerically robust estimate of NAC for NAMD.

3. Decoherence time

A known limitation of conventional fewest-switches surface hopping is "overcoherence", i.e., the persistence of electronic superpositions longer than physically justified in condensed phases. Decoherence-corrected schemes such as DISH address this issue by introducing a decoherence time τ_{ij} that sets the characteristic timescale for the decay of coherence between states i and j.

Within the commonly adopted Gaussian treatment of energy-gap fluctuations, decoherence is characterized through the decoherence function $D_{ij}(t)$, constructed from fluctuations of the instantaneous energy gap $E_{ij}(t) = E_j(t) - E_i(t)$. Defining $\delta E_{ij}(t) = E_{ij}(t) - \langle E_{ij}(t) \rangle$, the unnormalized autocorrelation function is:

$$C_{ij}(t) = \left\langle \delta E_{ij}(t') \delta E_{ij}(t - t') \right\rangle_t \#(4)$$

and the cumulant expression for the decoherence function reads:[16, 17]

$$D_{ij}(t) = \exp\left(-1/\hbar^2\right) \int_0^t dt' \int_0^{t'} dt'' C_{ij}(t'') \#(5)$$

In practice, $D_{ij}(t)$ is often well described by a Gaussian decay, from which an effective decoherence time τ_{ij} is extracted:

$$D_{ij}(t) = \exp\left(-\frac{t^2}{2\tau_{ij}^2}\right) \#(6)$$

Here, the initial magnitude of gap fluctuations $C_{ij}(0) = \delta\langle E_{ij}^2 \rangle$ and the decay behavior of $C_{ij}(t)$ jointly determine τ_{ij}: larger fluctuations and faster correlation loss generally correspond to shorter decoherence times, implying a more rapid collapse of electronic coherence in DISH.

4. Rabi period

The Rabi period (T_R) is defined as the time it takes for a quantum system to complete one full cycle of oscillation between two energy levels due to the interaction with an external perturbation, such as an electromagnetic field.[18-20] This period is inversely related to the Rabi frequency (Ω), which is a measure of the strength of the coupling between the two levels. The Ω is calculated using the NAC strength d_{ij} and energy separation ΔE between the two levels:

$$\Omega = \frac{\sqrt{{d_{ij}}^2 + \Delta E^2}}{\hbar} \#(7)$$

where d_{ij} represents the NAC matrix elements, ΔE is the energy separation between the two states, and $\hbar$ is the reduced Planck constant. The T_R is given by:

$$T_R = \frac{2\pi}{\Omega} \#(8)$$

The Rabi period plays a pivotal role in determining whether a system exhibits quantum Zeno or anti-Zeno behavior.[20] In the quantum Zeno effect,[21] frequent measurements or rapid decoherence can effectively "freeze" the system in its initial state, suppressing transitions between energy levels. Conversely, in the quantum anti-Zeno effect,[22, 23] infrequent measurements or slower decoherence can accelerate transitions, as the system has more time to evolve between states before being measured again. This analysis provides insights into the coherent oscillatory behavior of the system between two energy levels and is crucial for understanding whether the transitions in a system are affected by the quantum Zeno effect or the anti-Zeno effect.

Table S1. Formation energies E_{form} (eV) for the C, N, F, P, S, Cl, Se, Br and I doped brookite, anatase and rutile TiO_2, respectively.

Dopant	Brookite TiO_2	Anatase TiO_2	Rutile TiO_2

	O rich	Ti rich	O rich	Ti rich	O rich	Ti rich
C	8.36	4.77	8.42	5.21	8.84	5.61
N	5.01	1.42	5.05	1.83	5.10	1.86
F	-0.10	-3.69	0.01	-3.21	0.15	-3.09
P	7.34	3.75	7.75	4.54	8.55	5.32
S	4.62	1.03	4.77	1.56	5.72	2.48
Cl	3.83	0.24	4.20	0.99	4.89	1.66
Se	5.86	2.27	6.06	2.84	7.36	4.12
Br	5.37	1.78	5.99	1.89	6.91	3.67
I	8.02	4.43	8.41	5.19	10.49	7.25

Table S2. Carrier lifetimes in spin-up and spin-down channels for the M/TiO_2 systems (M = C, N, F, P, S, Cl, Se, Br and I).

	Spin-up		Spin-down	
System	τ_e (ns)	τ_h (ns)	τ_e (ns)	τ_h (ns)
C/TiO_2	3.24	5.47	0.40	0.33
N/TiO_2	60.39	60.39	2.71	2.92
F/TiO_2	15.07	13.31	53.12	53.12
P/TiO_2	1.30	2.12	0.32	0.31
S/TiO_2	6.90	9.89	Null	Null
Cl/TiO_2	42.97	29.05	99.04	99.14
Se/TiO_2	3.81	4.06	Null	Null
Br/TiO_2	30.11	19.88	37.23	37.28
I/TiO_2	2.92	3.61	6.98	15.27

Table S3. Canonically state-to-state times and transition rates (v), average energy separations (ΔE), averaged absolute NAC and decoherence time (τ_{ij}) for the spin-up and spin-down channels in C/TiO_2.

		ν (ns^{-1})	ΔE (eV)	NAC (meV)	τ_{ij} (fs)
Spin-up	CBM–VBM	0.012	2.43	0.61	14.04
	CBM–DL1	0.047	1.95	0.66	5.17
	CBM–DL2	0.073	0.74	0.56	4.50
	CBM–DL3	0.210	0.29	0.90	4.19
	DL3–VBM	0.704	2.15	0.92	4.33
	DL3–DL1	4.633	1.66	2.15	7.13
	DL3–DL2	16.047	0.45	2.69	7.02
	DL2–VBM	240.395	1.69	3.84	4.55
	DL2–DL1	2123.651	1.21	9.64	8.26
	DL1–VBM	3523.309	0.48	15.35	5.15
Spin-down	CBM–VBM	0.014	2.43	0.57	13.18
	CBM–DL4	0.111	1.95	0.72	4.63
	CBM–DL5	9.042	0.74	1.43	3.94
	CBM–DL6	2749.720	0.29	9.05	4.64
	DL6–VBM	0.025	2.15	0.36	4.28
	DL6–DL4	0.222	1.66	1.30	7.88
	DL6–DL5	26.351	0.45	2.51	7.39
	DL5–VBM	0.081	1.69	0.40	3.65
	DL5–DL4	2.912	1.21	0.90	7.76
	DL4–VBM	60.182	0.48	2.20	4.18

Table S4. Canonically state-to-state times and transition rates (ν), ΔE, averaged absolute NAC and τ_{ij} for the spin-up and spin-down channels in N/TiO_2.

		ν (ns^{-1})	ΔE (eV)	NAC (meV)	τ_{ij} (fs)
Spin-up	CBM–VBM	0.017	2.37	0.66	11.55
Spin-down	CBM–VBM	0.019	2.31	0.62	6.03
	CBM–DL1	0.392	1.37	0.88	3.06
	DL1–VBM	2.078	0.94	1.58	4.79

Table S5. Canonically state-to-state times and transition rates (ν), ΔE, averaged absolute NAC and τ_{ij} for the spin-up and spin-down channels in F/TiO_2.

		ν	ΔE	NAC	τ_{ij}

		(ns^{-1})	(eV)	(meV)	(fs)
Spin-up	CBM–VBM	0.011	2.57	0.57	13.00
	CBM–DL1	1342.282	0.26	11.97	19.17
	DL1–VBM	0.056	2.31	0.91	10.06
Spin-down	CBM–VBM	0.019	2.52	0.9	16.79

Table S6. Canonically state-to-state times and transition rates (ν), ΔE, averaged absolute NAC and τ_{ij} for the spin-up and spin-down channels in P/TiO_2.

		ν (ns^{-1})	ΔE (eV)	NAC (meV)	τ_{ij} (fs)
Spin-up	CBM–VBM	0.012	2.46	0.73	26.46
	CBM–DL1	0.072	1.83	0.49	4.38
	CBM–DL2	0.384	1.33	0.71	4.87
	CBM–DL3	0.638	1.12	0.98	5.29
	DL3–VBM	0.193	1.34	0.48	4.86
	DL3–DL1	7.683	0.70	2.25	4.92
	DL3–DL2	1104.413	0.21	5.73	6.58
	DL2–VBM	0.508	1.13	0.88	4.55
	DL2–DL1	90.997	0.50	3.94	5.90
	DL1–VBM	16.144	0.64	1.14	4.08
Spin-down	CBM–VBM	0.009	2.47	0.72	27.02
	CBM–DL4	0.079	1.71	0.53	4.21
	CBM–DL5	0.483	1.19	0.72	4.70
	CBM–DL6	592.901	0.34	4.03	5.23
	DL6–VBM	0.074	2.13	0.32	4.85
	DL6–DL4	1.087	1.37	1.81	5.02
	DL6–DL5	24.508	0.85	2.61	6.90
	DL5–VBM	0.373	1.28	0.77	4.45
	DL5–DL4	61.847	0.52	3.74	5.97
	DL4–VBM	6.114	0.76	0.92	3.98

Table S7. Canonically state-to-state times and transition rates (ν), ΔE, averaged absolute NAC and τ_{ij} in S/TiO_2.

	ν	ΔE	NAC	τ_{ij}

	(ns^{-1})	(eV)	(meV)	(fs)
CBM–VBM	0.013	2.39	0.58	11.18
CBM–DL1	0.017	2.12	0.51	5.52
CBM–DL2	0.233	1.72	0.79	4.41
DL2–VBM	25.938	0.67	2.65	4.54
DL2–DL1	215.950	0.40	4.83	6.44
DL1–VBM	2822.412	0.27	11.82	6.76

Table S8. Canonically state-to-state times and transition rates (ν), ΔE, averaged absolute NAC and τ_{ij} for the spin-up and spin-down channels in Cl/TiO_2.

		ν (ns^{-1})	ΔE (eV)	NAC (meV)	τ_{ij} (fs)
Spin-up	CBM–VBM	0.010	2.54	0.54	13.55
	CBM–DL1	1895.486	0.25	13.82	18.23
	DL1–VBM	0.024	2.30	0.57	9.87
Spin-down	CBM–VBM	0.010	2.51	0.64	17.43

Table S9. Canonically state-to-state times and transition rates (ν), ΔE, averaged absolute NAC and τ_{ij} in Se/TiO_2.

	ν (ns^{-1})	ΔE (eV)	NAC (meV)	τ_{ij} (fs)
CBM–VBM	0.010	2.46	0.69	20.23
CBM–DL1	0.035	2.15	0.64	5.13
CBM–DL2	0.042	1.77	0.56	4.66
CBM–DL3	0.314	1.37	0.83	4.76
DL3–VBM	0.327	1.08	0.74	4.38
DL3–DL1	13.961	0.77	2.94	5.78
DL3–DL2	344.453	0.39	5.54	6.46
DL2–VBM	13.055	0.69	1.78	4.61
DL2–DL1	603.598	0.38	7.49	5.72
DL1–VBM	1061.751	0.31	6.48	5.03

Table S10. Canonically state-to-state times and transition rates (ν), ΔE, averaged absolute NAC and τ_{ij} for the spin-up and spin-down channels in Br/TiO_2.

		ν (ns^{-1})	ΔE (eV)	NAC (meV)	τ_{ij} (fs)
Spin-up	CBM–VBM	0.018	2.46	0.52	8.27
	CBM–DL1	1727.665	0.25	12.13	11.87
	DL1–VBM	0.033	2.20	0.59	6.36
Spin-down	CBM–VBM	0.027	2.42	0.62	8.28

Table S11. Canonically state-to-state times and transition rates (ν), ΔE, averaged absolute NAC and τ_{ij} for the spin-up and spin-down channels in I/TiO_2.

		ν (ns^{-1})	ΔE (eV)	NAC (meV)	τ_{ij} (fs)
Spin-up	CBM–VBM	0.012	2.56	0.60	12.37
	CBM–DL1	0.032	2.35	0.46	5.90
	CBM–DL2	0.076	2.07	0.61	4.93
	CBM–DL3	0.060	1.85	0.61	4.92
	CBM–DL4	2561.678	0.27	12.46	6.84
	DL4–VBM	0.042	2.29	0.61	4.97
	DL4–DL1	0.089	2.08	0.62	4.35
	DL4–DL2	0.162	1.80	0.69	3.84
	DL4–DL3	0.390	1.58	0.87	3.69
	DL3–VBM	3.031	0.72	1.38	5.51
	DL3–DL1	81.113	0.51	4.56	6.01
	DL3–DL2	3043.518	0.22	14.26	6.34
	DL2–VBM	75.643	0.50	2.62	5.47
	DL2–DL1	1593.499	0.29	9.96	6.63
	DL1–VBM	4168.188	0.21	14.45	6.92
Spin-down	CBM–VBM	0.013	2.56	0.69	15.18
	CBM–DL5	0.013	2.34	0.51	6.11
	CBM–DL6	0.025	2.05	0.56	5.15
	CBM–DL7	0.096	1.83	0.69	5.22
	DL7–VBM	2.934	0.72	1.36	5.52
	DL7–DL5	80.396	0.51	4.59	6.14
	DL7–DL6	3099.718	0.22	14.36	6.44
	DL6–VBM	62.216	0.50	2.51	5.47
	DL6–DL5	1607.077	0.29	10.03	6.60
	DL5–VBM	4125.534	0.22	13.75	6.76

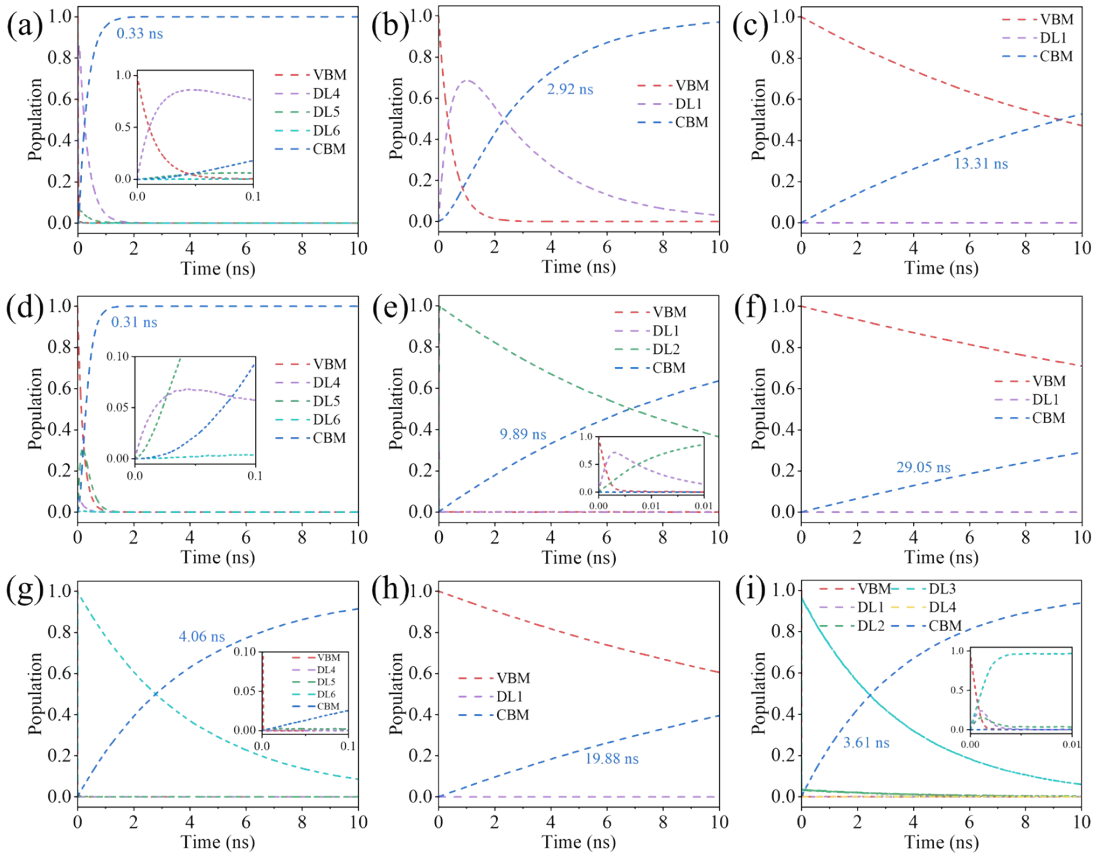

Fig. S1 Time evolution of hole populations between the band edge and the defect levels at 300 K for brookite TiO_2 doped with nonmetal atoms: (a) C, (b) N, (c) F, (d) P, (e) S, (f) Cl, (g) Se, (h) Br and (i) I.

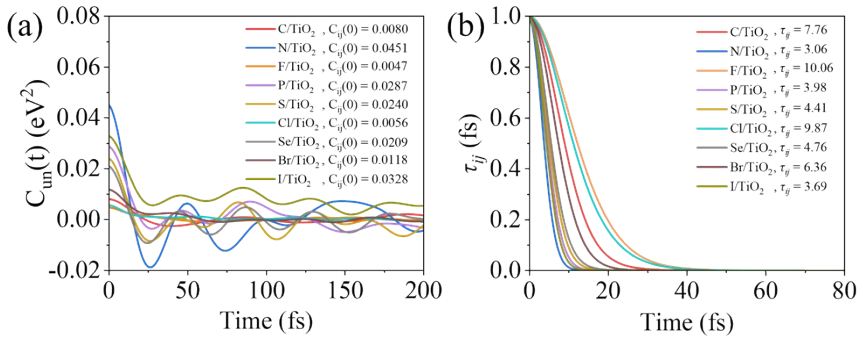

Fig. S2 (a) Unnormalized autocorrelation functions and (b) decoherence functions in different nonmetal doped brookite TiO_2 systems.

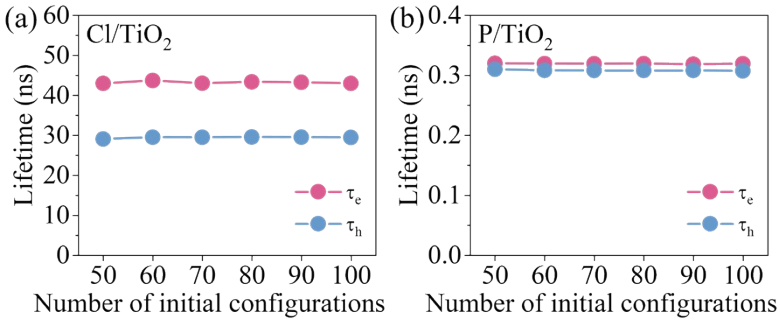

Fig. S3 Convergence of fitted carrier lifetimes with respect to the number of initial configurations for representative system (a) Cl/TiO_2 and (b) P/TiO_2.

References

1. G. Kresse and J. Furthmüller, *Phys. Rev. B*, 1996, **54**, 11169.
2. J. P. Perdew, K. Burke and M. Ernzerhof, *Phys. Rev. Lett.*, 1996, **77**, 3865-3868.
3. D. J. Chadi and M. L. Cohen, *Phys. Rev. B*, 1973, **8**, 5747-5753.
4. P. R. Varadwaj, V. A. Dinh, Y. Morikawa and R. Asahi, *ACS omega*, 2023, **8**, 22003-22017.
5. N. A. Johari, N. Hamzah, A. F. A. Faizal, M. H. Samat, O. H. Hassan, A. M. M. Ali, M. Z. A. Yahya and M. F. M. Taib, *Mater. Today Proc.*, 2022, **66**, 4061-4067.
6. S. B. Zhang and J. E. Northrup, *Phys. Rev. Lett.*, 1991, **67**, 2339.
7. C. Freysoldt, B. Grabowski, T. Hickel, J. Neugebauer, G. Kresse, A. Janotti and C. G. Van de Walle, *Rev. Mod. Phys.*, 2014, **86**, 253-305.
8. G. Ren, M. Zhou and H. Wang, *J. Am. Chem. Soc.*, 2024, **146**, 6084-6093.
9. R. Asahi, T. Morikawa, T. Ohwaki, K. Aoki and Y. Taga, *Science*, 2001, **293**, 269-271.
10. A. Mittal, B. Mari, S. Sharma, V. Kumari, S. Maken, K. Kumari and N. Kumar, *J. Mater. Sci.: Mater. Electron.*, 2019, **30**, 3186-3207.
11. Y. Wang, J. Chen, X. Zhang, Y. Yang, Q. Yang, X. Liu, X. Tao, Y. Jin, G. Lu and X. Zhang, *Mater. Res. Bull.*, 2022, **155**, 111968.
12. Q. Zheng, W. Chu, C. Zhao, L. Zhang, H. Guo, Y. Wang, X. Jiang and J. Zhao, *WIREs Comput. Mol. Sci.* , 2019, **9**, e1411.
13. C. F. Craig, W. R. Duncan and O. V. Prezhdo, *Phys. Rev. Lett.*, 2005, **95**, 163001.
14. J. C. Tully, *J. Chem. Phys.*, 1990, **93**, 1061-1071.
15. C. Zhang, Y. Zhong, Z.-G. Tao, X. Qin, H. Shang, Z. Lan, O. V. Prezhdo, X.-G. Gong, W. Chu and H. Xiang, *Nat. Commun.*, 2025, **16**, 2033.
16. G. Lau, H. Xu, Y. Li, K. Ding, Y. Zhang and W. Lin, *Adv. Funct. Mater.*, 2025, **35**, 2503757.
17. A. V. Akimov and O. V. Prezhdo, *J. Phys. Chem. Lett.*, 2013, **4**, 3857-3864.
18. D. A. Tumakov, D. A. Telnov, G. Plunien and V. M. Shabaev, *Phys. Rev. A*, 2019, **100**, 023407.
19. C. D. Parmee and N. R. Cooper, *Phys. Rev. A*, 2018, **97**, 053616.
20. S. Gumber and O. V. Prezhdo, *J. Phys. Chem. Lett.*, 2023, **14**, 7274-7282.
21. B. Misra and E. C. G. Sudarshan, *J. Math. Phys.*, 1977, **18**, 756-763.
22. A. G. Kofman and G. Kurizki, *Nature*, 2000, **405**, 546-550.
23. P. Facchi, H. Nakazato and S. Pascazio, *Phys. Rev. Lett.*, 2001, **86**, 2699-2703.